

# Sinter-resistant metal nanoparticle catalysts achieved by immobilization within zeolite crystals via seed-directed growth

Jian Zhang<sup>1,2,3</sup>, Liang Wang<sup>1,3\*</sup>, Bingsen Zhang<sup>4</sup>, Haishuang Zhao<sup>5</sup>, Ute Kolb<sup>5</sup>, Yihan Zhu<sup>6,7</sup>, Lingmei Liu<sup>6</sup>, Yu Han<sup>6</sup>, Guoxiong Wang<sup>1,3</sup>, Chengtao Wang<sup>1,3</sup>, Dang Sheng Su<sup>4</sup>, Bruce C. Gates<sup>8</sup> and Feng-Shou Xiao<sup>1,2,3\*</sup>

**Supported metal nanoparticle catalysts are widely used in industry but suffer from deactivation resulting from metal sintering and coke deposition at high reaction temperatures. Here, we show an efficient and general strategy for the preparation of supported metal nanoparticle catalysts with very high resistance to sintering by fixing the metal nanoparticles (platinum, palladium, rhodium and silver) with diameters in the range of industrial catalysts (0.8–3.6 nm) within zeolite crystals (metal@zeolite) by means of a controllable seed-directed growth technique. The resulting materials are sinter resistant at 600–700 °C, and the uniform zeolite micropores allow for the diffusion of reactants enabling contact with the metal nanoparticles. The metal@zeolite catalysts exhibit long reaction lifetimes, outperforming conventional supported metal catalysts and commercial catalysts consisting of metal nanoparticles on the surfaces of solid supports during the catalytic conversion of C<sub>1</sub> molecules, including the water-gas shift reaction, CO oxidation, oxidative reforming of methane and CO<sub>2</sub> hydrogenation.**

Noble metals are dominant among catalysts used for technological applications. Because they are expensive, dispersions in the form of nanoparticles on porous supports are often used to maximize the metal surface area and the number of atoms accessible for catalysis<sup>1–3</sup>. A major challenge during application is catalyst deactivation, which results from metal sintering and surface area loss, accompanied by the formation of surface-covering deposits of coke<sup>3–14</sup>. Regeneration of supported metal catalysts is complex and expensive, often requiring metal leaching, purification and redeposition<sup>15,16</sup>. To minimize sintering, researchers have learned to strengthen metal–support interactions<sup>6,7,9,12</sup> and, alternatively, have coated the metals with thin shells of porous oxides<sup>17–22</sup> or carbon<sup>23</sup>. However, the pores are poorly controlled, and many active sites remain covered and do not participate in reactions. Researchers have addressed this challenge by encapsulating metal catalysts in materials with small, stable, rigid and uniform pores—zeolites<sup>24,25</sup>—to hinder sintering and provide access through three-dimensional (3D) pore networks<sup>26–28</sup>. In these cases, organic additives (for example, sulphur- or nitrogen-containing organic compounds) are necessary for stabilizing metal species during the zeolite crystallization, because the metal species easily aggregate into larger particles under the harsh crystallization conditions (for example, high temperature and strong basicity). These general routes fail to control the diameters of the metal nanoparticles, which are either smaller than the diameters of the zeolite cavities or larger than 5 nm. To date, it is still challenging to fix metal nanoparticles with controllable sizes inside zeolite crystals;

for example, to create desirable diameters in the range of industrial catalysts (that is, 1.5–4.0 nm)<sup>29–32</sup>.

Here, we demonstrate a general methodology for zeolite encapsulation of metal nanoparticles to prevent metal sintering. The key for the preparation of these metal@zeolite catalysts is the use of zeolite seeds that already contain metal nanoparticles, and which are then placed into aluminosilicate or silicate gels to form a crystalline zeolite sheath around the metal-containing seeds. This strategy works without the use of organic stabilizers and leads to metal nanoparticles in the widely useful size range of 0.8–3.6 nm. The resultant catalysts exhibit extraordinary sinter resistance in the high-temperature water-gas shift (WGS) reaction at 300 °C, CO oxidation at 200 °C, oxidative reforming of methane at 600 °C and CO<sub>2</sub> hydrogenation at 350 °C.

## Results

**Synthesis and characterization.** A model of metal@zeolite catalysts and catalytic strategy is presented in Fig. 1. Zeolite seeds are critical in the synthesis (Supplementary Fig. 1); if they are absent from the starting gels, the resultant encapsulated metal nanoparticles have larger sizes<sup>33,34</sup>. In this work, platinum, palladium, rhodium and silver nanoparticles were loaded onto the surfaces of the zeolite seeds (Supplementary Fig. 2), then used for seed-directed growth to give larger zeolite crystals. The resultant structures include the zeolites Beta and MOR, as well as pure-silica silicalite-1 (S-1) zeolites. Thus, Pt@Beta (Fig. 2 and Supplementary Fig. 3), Pt@MOR (Supplementary Fig. 4), Ag@Beta (Supplementary Fig. 5), Ag@

<sup>1</sup>Key Laboratory of Applied Chemistry of Zhejiang Province, Zhejiang University, Hangzhou, China. <sup>2</sup>Beijing Advanced Innovation Center for Soft Matter Science and Engineering, Beijing University of Chemical Technology, Beijing, China. <sup>3</sup>Department of Chemistry, Zhejiang University, Hangzhou, China.

<sup>4</sup>Shenyang National Laboratory of Materials Science, Institute of Metal Research, Chinese Academy of Sciences, Shenyang, China. <sup>5</sup>Institute of Inorganic Chemistry and Analytical Chemistry, Johannes Gutenberg University Mainz, Mainz, Germany. <sup>6</sup>Advanced Membranes and Porous Materials Center, Physical Sciences and Engineering Division, King Abdullah University of Science and Technology, Thuwal, Saudi Arabia. <sup>7</sup>Department of Chemical Engineering, Zhejiang University of Technology, Hangzhou, China. <sup>8</sup>Department of Chemical Engineering, University of California, Davis, Davis, CA, USA.

\*e-mail: [liangwang@zju.edu.cn](mailto:liangwang@zju.edu.cn); [fsxiao@zju.edu.cn](mailto:fsxiao@zju.edu.cn)

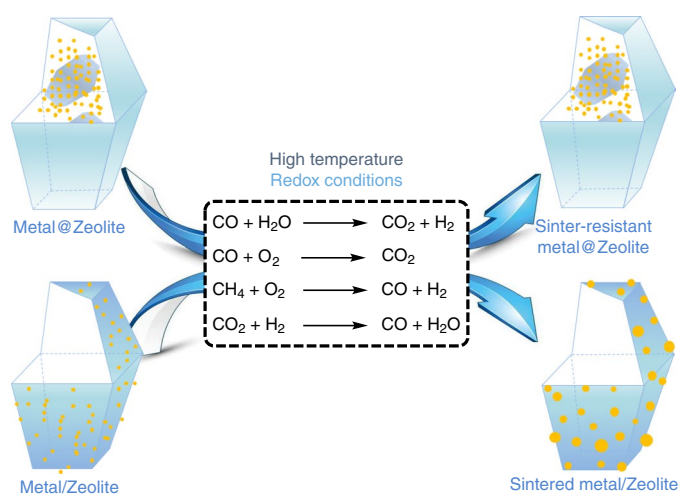


**Fig. 1 | Schematic model of metal nanoparticles fixed within and on the outer surfaces of zeolite crystals.** The metal nanoparticles (yellow) in metal@zeolite catalysts are sinter resistant, whereas those in metal/zeolite catalysts easily aggregate into larger particles in the WGS, CO oxidation, oxidative reforming of methane and  $\text{CO}_2$  hydrogenation reactions.

MOR (Supplementary Fig. 6), Rh@Beta (Supplementary Fig. 7), Rh@MOR (Supplementary Fig. 8) and Pd@S-1 (Supplementary Fig. 9) were prepared. The metal loadings (0.39–1.01 wt% by inductively coupled plasma analysis) are summarized in Supplementary Table 1. Notably, these syntheses were performed in the absence of organic stabilizers, which makes them environmentally friendly. Significantly, the sizes of metal nanoparticles on the zeolite seeds could be adjusted. Consequently, the sizes of the metal nanoparticles in the final metal@zeolite catalysts are controllable, as shown, for example, for Pt@Beta (platinum nanoparticle diameter range: 0.8–3.2 nm; mean diameter: 1.6 nm (Fig. 2c); platinum nanoparticle diameter distribution: 1.2–3.6 nm; mean diameter: 2.0 nm (Supplementary Fig. 10a); platinum size distribution: 1.6–6.0 nm; mean diameter: 3.6 nm (Supplementary Fig. 10c)). More importantly, this route is general, allowing stable fixation of silver, rhodium and palladium nanoparticles in the zeolite crystals (Supplementary Figs. 11–13 and Supplementary Table 1), making the method superior to state-of-the-art techniques.

Figure 2a represents Pt@Beta schematically. The platinum nanoparticles are firmly fixed within the zeolite Beta crystals. Scanning transmission electron microscopy (STEM) (Fig. 2b) and high-resolution transmission electron microscopy (HR-TEM) (Fig. 2c) images of Pt@Beta provide direct evidence of the nanoparticles in the 0.8–3.2 nm size range. Characterizations with scanning electron microscopy (SEM) (inset in Fig. 2b), X-ray diffraction crystallography (Supplementary Fig. 3) and  $\text{N}_2$  sorption isotherms (Supplementary Fig. 14) show that Pt@Beta has high purity and crystallinity. The STEM image of Pt@Beta shows the distribution of metal nanoparticle diameters in the zeolite crystals (Fig. 3a), where region I in the image is rich in platinum nanoparticles and region II has almost none observable, indicating a non-uniform distribution of platinum nanoparticles. Because the outline of region I has a shape similar to that of a zeolite crystal, we infer that the Pt/Beta zeolite seed (region I) was localized within the newly formed zeolite Beta framework that encapsulated it (region II).

We propose that the platinum-containing zeolite seed (Pt/Beta seed) directed the growth of zeolite crystals during the synthesis of Pt@Beta, as confirmed by the transmission electron microscopy (TEM) characterization of the crystallization process of the Pt@Beta sample (Supplementary Figs. 15–23). Thus, the newly formed

zeolite grows around the seed crystals, supporting platinum nanoparticles and fixing them inside the newly formed zeolite framework (Fig. 3b,c and Supplementary Figs. 22 and 24), leading to a significantly lower platinum loading of Pt@Beta (0.41 wt%) compared with the Pt/Beta seed (2.0 wt%). Owing to the significantly different Si/Al ratio between the Pt/Beta seed (Si/Al ratio: ~12) and the newly formed zeolite Beta framework or amorphous Si–Al gel (Si/Al ratio: ~5.3), the location of the zeolite seeds in the final Pt@Beta crystals was also identifiable by energy dispersive spectrometry analysis, indicating the distinguishable Si/Al ratios (Supplementary Fig. 22b). As shown in the STEM image (Supplementary Fig. 22), the region with brighter contrast is obviously surrounded by less bright regions. The energy dispersive spectrometry analysis demonstrates that the Si/Al ratio in the bright region (region 2 in Supplementary Fig. 22a) is obviously higher than in the less bright region (regions 1 and 3 in Supplementary Fig. 22a). Similar results were also observed in randomly selected regions of Pt@Beta samples crystallized at various times (Supplementary Figs. 19–21), indicating that the seeds are encapsulated by the Si–Al gel and/or newly formed Beta zeolite framework.

STEM images and nano electron diffraction data characterizing Pt@Beta crystallized for 4 h (for example, Fig. 3d,e) and containing partially crystallized Pt@Beta and still unconverted amorphous aluminosilicate gel show significantly different contrasts. The zeolite seeds are covered in aluminosilicate gel in a core–shell structure (Fig. 3d) that is evidenced by a series of tilt images (from  $-70^\circ$  to  $70^\circ$  with  $1^\circ$  intervals; Supplementary Video 1). These data further confirm the proposed core–shell growth mechanism directed by the platinum-containing zeolite seeds, whereby the amorphous aluminosilicate covers the seeds and isolates individual platinum nanoparticles (Supplementary Video 1 and Supplementary Fig. 23), thus hindering their aggregation during the crystallization process (Supplementary Videos 2–4; Pt@Beta is shown with a platinum nanoparticle diameter of 0.8–3.2 nm in Supplementary Video 2 and 1.6–6.0 nm in Supplementary Videos 3 and 4).

In contrast, a conventional Beta-zeolite-supported platinum nanoparticle catalyst (Pt/Beta) was prepared by the impregnation method to have a platinum loading of 0.98 wt% and found to incorporate platinum nanoparticles only on the external zeolite surface (Fig. 2e–g).

Our synthesis strategy extends to other samples, illustrated by Pt@MOR (Supplementary Fig. 4a,b), Ag@Beta (Supplementary Fig. 5a,b), Ag@MOR (Supplementary Fig. 6a,b), Rh@Beta (Supplementary Fig. 7a,b), Rh@MOR (Supplementary Fig. 8a,b) and Pd@S-1 (Supplementary Fig. 9). Again, the TEM tomographic images (Supplementary Fig. 25) show that the metal nanoparticles are enveloped by the zeolite crystals.

**Stability evaluation.** Figure 2d shows a TEM tomographic image of Pt@Beta calcined at  $600^\circ\text{C}$  for 240 min in air—conditions that challenge the survival of nano-sized metal particles<sup>3,28</sup>. Significantly, the platinum nanoparticles in this calcined Pt@Beta remained in the 0.8–3.2 nm diameter range, matching that of the as-synthesized Pt@Beta. Equivalent results were observed for Pt@MOR, Ag@Beta, Ag@MOR, Rh@Beta, Rh@MOR and Pd@S-1 (Supplementary Fig. 26), demonstrating the outstanding resistance of each of them to thermal sintering. These data confirm that the rigid zeolite framework fixes the metal nanoparticles, preventing their sintering. In contrast, the metal nanoparticles on the external surfaces of zeolite crystals readily aggregate into larger metal particles after the same treatments (Fig. 2h, Supplementary Figs. 27 and 28, and Supplementary Videos 5–7).

The zeolite provides not only a stabilizing matrix for the metal nanoparticles but also channels in the open micropore system that allow access of reactant molecules to the metal sites, facilitating catalysis<sup>35–39</sup>. This point is illustrated by the data of Fig. 4a

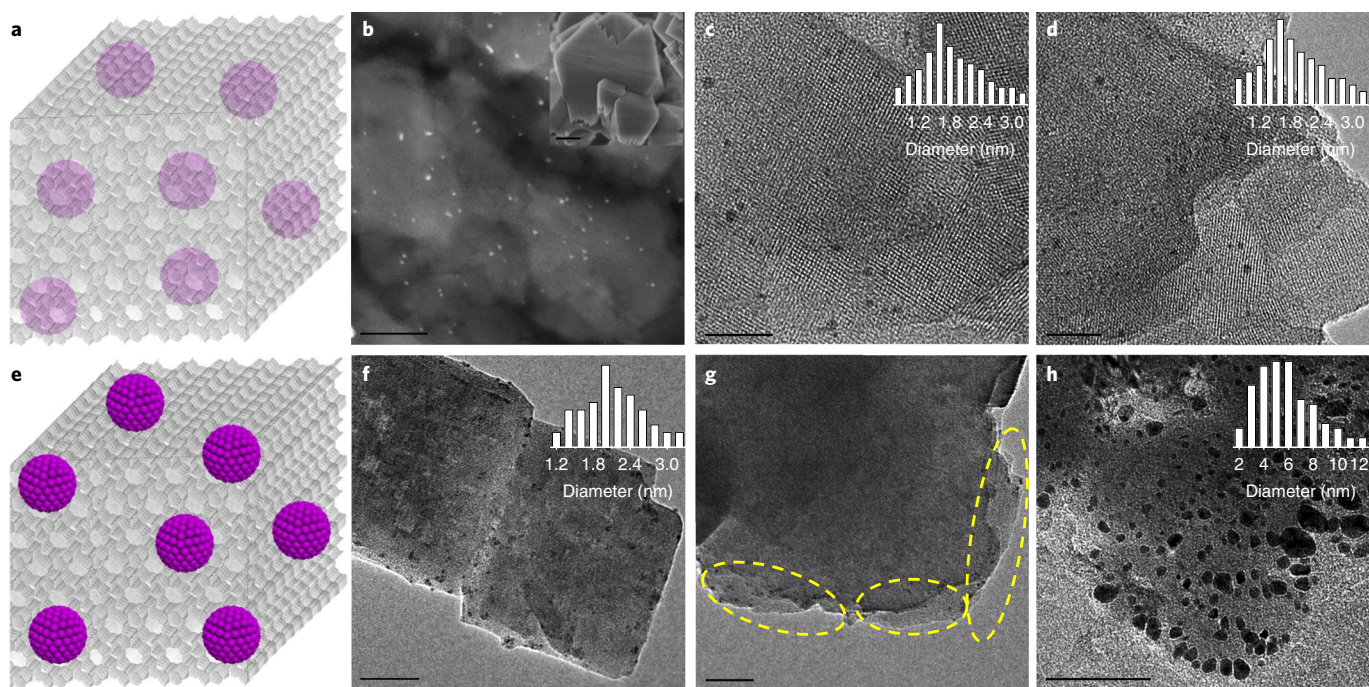


**Fig. 2 | TEM images of supported platinum catalysts. a–c,** Proposed model (a), STEM image (b) and HR-TEM tomographic image (c) of Pt@Beta. **d,** HR-TEM tomographic image of Pt@Beta after calcination at 600 °C for 240 min. **e–g,** Proposed model (e), TEM image (f) and TEM tomographic image (g) of Pt/Beta. **h,** TEM image of Pt/Beta after calcination at 600 °C for 240 min. Inset in **b:** SEM image of Pt@Beta. Insets in **c, d, f** and **h:** platinum nanoparticle size distributions. The yellow ellipses in **g** highlight the platinum nanoparticles. Scale bars: 50 nm in **b, f, g** and **h,** 20 nm in **c** and **d,** and 200 nm in the inset in **b.**

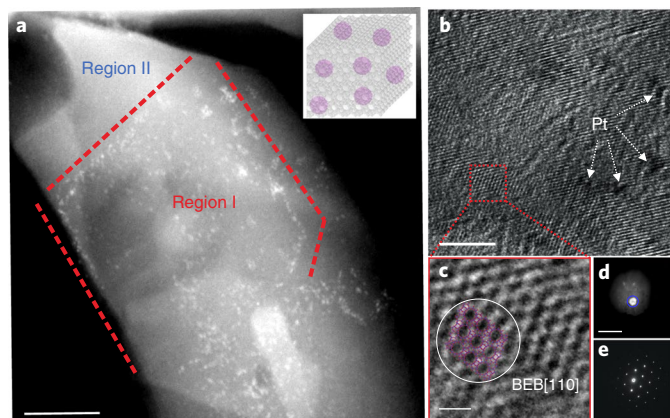


**Fig. 3 | TEM characterization of Pt@Beta. a,** STEM image characterizing the platinum nanoparticle distribution. Region I is rich in platinum nanoparticles and region II has almost none observable. The dashed line shows the boundary of Region I. The inset shows the model of the Pt@Beta sample. **b,** HR-TEM image of Pt@Beta. **c,** Enlarged view of the red square in **b.** The white circle highlights the microdomains of polymorph B (BEB) of zeolite Beta, overlaid by a BEB structure model viewed along [110]. **d,** STEM image of a Pt@Beta sample crystallized at 4 h. **e,** Corresponding electron diffraction pattern of the circle in **d.** Scale bars: 50 nm in **a,** 20 nm in **b,** 25 Å in **c** and 500 nm in **d.**

showing the dependence of catalytic activity on reaction temperature in the WGS reaction catalysed by Pt@Beta (the catalyst incorporated platinum particles 0.8–3.2 nm in diameter) and, for comparison, Pt/Beta. The two catalysts have almost the same average rates in the temperature range 200–400 °C, but their catalytic stabilities differ markedly. After a reaction time of

6,000 min (Fig. 4b), Pt@Beta remained highly active (average rate:  $561 \text{ mol}_{\text{CO}} \text{ mol}_{\text{Pt}}^{-1} \text{ h}^{-1}$ ), having lost only about 10% of its activity (the average reaction rate of the fresh catalyst was  $615 \text{ mol}_{\text{CO}} \text{ mol}_{\text{Pt}}^{-1} \text{ h}^{-1}$ ). In contrast, after reaction for 2,640 min, the conventional Pt/Beta catalyst was sharply deactivated, with the average rate decreasing from 630 to  $435 \text{ mol}_{\text{CO}} \text{ mol}_{\text{Pt}}^{-1} \text{ h}^{-1}$ . TEM images show that the used Pt@Beta still incorporated platinum nanoparticles in the original diameter range of 0.8–3.2 nm (Supplementary Fig. 29), whereas the used Pt/Beta incorporated much larger nanoparticles (2–8 nm; Supplementary Fig. 30).

Significantly, calcination in air of the used Pt@Beta brought the activity ( $610 \text{ mol}_{\text{CO}} \text{ mol}_{\text{Pt}}^{-1} \text{ h}^{-1}$ ) back, within error, to the value characterizing the fresh catalyst ( $615 \text{ mol}_{\text{CO}} \text{ mol}_{\text{Pt}}^{-1} \text{ h}^{-1}$ ) because the carbonaceous deposits (coke) that had accumulated on the active sites were burned off. The full regeneration of the activity demonstrates the superior stability of the Pt@Beta catalyst; in contrast, the equivalent calcination of the used Pt/Beta catalyst led to a further reduction of its activity caused by further aggregation of the platinum nanoparticles. Even the catalyst recently reported by Liu et al.<sup>28</sup>, which consisted of pre-made platinum nanoclusters encapsulated in the siliceous zeolite MCM-22 (despite offering resistance to metal sintering under harsh conditions of reduction and oxidation at 650 °C) was characterized by some platinum sintering, as the smallest clusters aggregated into larger clusters with diameters in the range of 1–2 nm. This was accompanied by an approximately 10% loss of catalytic activity for propane dehydrogenation over five reaction–regeneration cycles<sup>28</sup>.

We carried out a further comparison with the commercial catalyst commercial Pt/ZSM-23 (Pt/ZSM-23-com—ZSM-23 zeolite-supported platinum nanoparticles; Supplementary Fig. 31), commercial Pt/Al<sub>2</sub>O<sub>3</sub> (Pt/Al<sub>2</sub>O<sub>3</sub>-com—Al<sub>2</sub>O<sub>3</sub>-supported platinum nanoparticles; Supplementary Fig. 32) and Pt/Beta-ion (zeolite-Beta-supported platinum synthesized by ion exchange of commercial zeolite Beta with Pt(NH<sub>3</sub>)<sub>4</sub>(NO<sub>3</sub>)<sub>2</sub>; Supplementary Fig. 33).

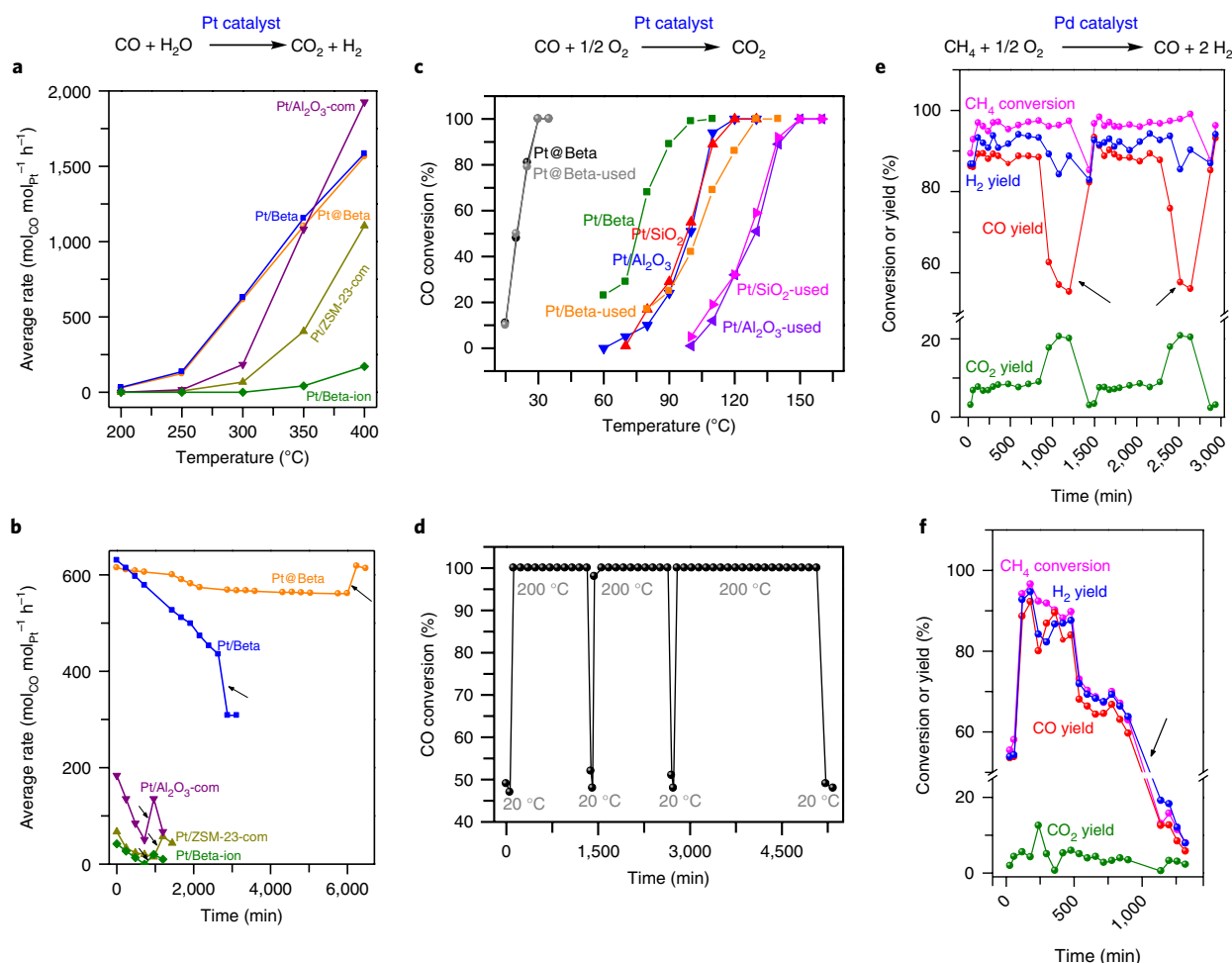


**Fig. 4 | Catalytic evaluation of metal@zeolite catalysts in flow reactors.** **a, b**, Average rates as a function of temperature (**a**) and time (**b**; at 300 °C) for reactions catalysed by various catalysts. Reaction conditions: 50 ml min<sup>-1</sup> of reaction gas (15% CO + 5% CO<sub>2</sub> + 30% H<sub>2</sub>O + 40% H<sub>2</sub> + 10% He); GHSV = 1,875,000 ml g<sub>Pt</sub><sup>-1</sup> h<sup>-1</sup>. The average rates with error within ±2% were calculated as the number of moles of converted CO per mole of platinum per hour. **c**, CO oxidation catalysed (at 350 °C for 1,200 min) by fresh and used Pt@Beta, Pt/Beta, Pt/SiO<sub>2</sub> and Pt/Al<sub>2</sub>O<sub>3</sub>. **d**, Conversion of CO catalysed by Pt@Beta as a function of time on stream at 200 °C. Reaction conditions: 20 ml min<sup>-1</sup> of reactant gas (1% CO + 19% O<sub>2</sub> + 80% He); GHSV = 120,000 ml g<sub>Pt</sub><sup>-1</sup> h<sup>-1</sup>. The errors of CO conversions were within ±2%. **e, f**, Oxidative reforming of methane catalysed by Pd@S-1 (**e**) and Pd/S-1 (**f**). Reaction conditions: 20 ml min<sup>-1</sup> of reactant gas (7% CH<sub>4</sub> + 3.3% O<sub>2</sub> + 79.7% He); GHSV = 480,000 ml g<sub>Pd</sub><sup>-1</sup> h<sup>-1</sup>; 600 °C. The errors of conversions and yields were within ±3%. The black arrows highlight the calcination treatment to regenerate the catalysts.

Testing these catalysts as mentioned above for the WGS reaction, we found that they all exhibited irreversible activity losses in quite short times of operation (<700 min) as a consequence of sintering of the platinum nanoparticles (Fig. 4b and Supplementary Figs. 31–34). Reductive pre-treatments (650 °C, H<sub>2</sub>, 600 min) were also performed with these catalysts to evaluate the sinter resistance of the platinum, and the data show that significant aggregation of the platinum nanoparticles occurred (Supplementary Figs. 31–33). In contrast, the platinum nanoparticle sizes of Pt@Beta were almost unchanged as a result of the same treatment in H<sub>2</sub>; Supplementary Fig. 35). The remarkable stability of Pt@Beta compared with the commercial catalysts in the WGS reaction indicates its potential technological value; for example, for the production of hydrogen from syngas, the purification of hydrogen in fuel cell applications and balancing of the H<sub>2</sub>/CO ratio in syngas<sup>40–43</sup>.

Further comparisons demonstrating the advantages of the Pt@Beta catalyst are illustrated by the data in Fig. 4c, which show the dependence of CO conversion on the reaction temperature for various catalysts, confirming the high activity of Pt@Beta. For example, Pt@Beta gives a CO conversion of 48% at 20 °C and >99%

conversion at 30 °C, whereas nearly complete conversion of CO with the conventional oxide-supported catalysts Pt/SiO<sub>2</sub> or Pt/Al<sub>2</sub>O<sub>3</sub> required temperatures >120 °C. Figure 4d shows the catalytic activity of Pt@Beta for CO oxidation at 200 °C in experiments in which the temperature was periodically decreased to 20 °C for short periods and then increased back to 200 °C. Pt@Beta is characterized by stable performance at both high and low temperatures. Furthermore, after reaction at 350 °C for 1,200 min, the used Pt@Beta catalyst was characterized by a CO conversion nearly matching that of the fresh catalyst (Fig. 4c). TEM images of the used Pt@Beta catalyst (Supplementary Fig. 36) provide evidence of a platinum nanoparticle size distribution matching that of the fresh catalyst (within error), indicating the extreme sinter resistance of the platinum nanoparticles in Pt@Beta. In contrast, the activities of the conventional catalysts (Pt/SiO<sub>2</sub> and Pt/Beta; Supplementary Figs. 37 and 38) decreased markedly in operation as a result of sintering of the platinum nanoparticles. Similar results were also obtained in experiments with the silver-catalysed CO oxidation. Ag@Beta displayed stable activity in a test for 2,880 min at 400 °C (Supplementary Fig. 39a), with the used catalyst having silver nanoparticle sizes

essentially unchanged from those of the fresh catalyst (Supplementary Fig. 40). In contrast, the activities of silver nanoparticles supported on Beta zeolite (Ag/Beta) and  $\text{Al}_2\text{O}_3$  (Ag/ $\text{Al}_2\text{O}_3$ ) by the impregnation method decreased markedly as a result of silver sintering (Supplementary Figs. 39b,c and 41). Thus, also for CO oxidation catalysis, our results demonstrate a strong resistance to sintering of metal nanoparticles, in contrast with the performance of conventional supported metal catalysts, which undergo sintering facilitated by  $\text{CO}^{44,45}$ .

Further evidence of the benefits of the new catalysts is demonstrated by the results obtained with samples incorporating promoters. For example, iron promoters increase the activities of platinum catalysts for CO oxidation<sup>46,47</sup>. We introduced iron cations into Pt@Beta by ion exchange to form Pt@Beta-Fe (1.49 wt% Fe), finding that this catalyst shows much higher activity than Pt@Beta, giving essentially complete conversion of CO at 25 °C (Supplementary Figs. 42 and 43).

Further results were obtained for oxidative reforming of methane—a typical high-temperature reaction that challenges catalyst stability<sup>48,49</sup>. Figure 4e,f and Supplementary Fig. 44 show the performance in oxidative reforming of methane catalysed by Pd@S-1 (Supplementary Figs. 3g, 9 and 45; the sample with a palladium particle diameter distribution of 0.8–3.0 nm), Pd@S-1 and commercial Pd/ $\text{Al}_2\text{O}_3$  (palladium nanoparticles supported on alumina, designated as Pd/ $\text{Al}_2\text{O}_3$ -com). At 600 °C, Pd@S-1 gives an initial methane conversion at 89%, and this value increased to 97% after an induction period of 120 min (Fig. 4e), with CO and  $\text{H}_2$  formed as major products (CO yield: 89%;  $\text{H}_2/\text{CO}$  ratio: 2.09) and a low  $\text{CO}_2$  yield (<8%). When the reaction catalysed by Pd@S-1 was carried out continuously for >960 min in a flow reactor, the CO yield decreased because of coke formation (confirmed by thermogravimetric analysis; Supplementary Fig. 46b), but a facile calcination in oxygen brought back the activity fully. Even after the reaction at 600 °C for 2,280 min, the palladium nanoparticle size distribution in Pd@S-1 still matched that of the fresh catalyst (Supplementary Fig. 47). In contrast, the conventionally made Pd/S-1 lost significant activity in a short time (Fig. 4f; 63% at 900 min) because of the combined effects of coke formation (Supplementary Fig. 46a) and palladium aggregation (Supplementary Fig. 48). Furthermore, the commercial Pd/ $\text{Al}_2\text{O}_3$ -com exhibited much lower selectivity for CO formation (54% with a  $\text{CH}_4$  conversion at 65.8%) than Pd@S-1, as a consequence of over-oxidation, to give  $\text{CO}_2$  (Supplementary Fig. 44). After oxidative reforming of methane at 600 °C for 840 min catalysed by Pd/ $\text{Al}_2\text{O}_3$ -com, the CO selectivity decreased to 41.4% with a  $\text{CH}_4$  conversion at 55.1% (Supplementary Fig. 44). A calcination treatment recovered 90% of the  $\text{CH}_4$  conversion, but the CO selectivity was much lower (42.2% after the second calcination) as a consequence of the aggregated palladium nanoparticles, shown by TEM (Supplementary Fig. 49). Thus, our data show that encapsulating metal nanoparticles in zeolites produces catalysts that offer the practical advantages of resistance to both coke formation and metal sintering.

Moreover, catalytic data were obtained for  $\text{CO}_2$  hydrogenation—a reaction used to convert this greenhouse gas into useful  $\text{CO}^{50}$ . Rh@Beta, Rh/Beta (rhodium nanoparticles supported on zeolite Beta by the impregnation method) and commercial Rh/ $\text{Al}_2\text{O}_3$  (denoted as Rh/ $\text{Al}_2\text{O}_3$ -com) catalysts were all found to be active for  $\text{CO}_2$  conversion, but with different selectivities (Supplementary Figs. 50 and 51). Methanation was the dominant reaction on Rh/ $\text{Al}_2\text{O}_3$  and Rh/Beta, with  $\text{CH}_4$  as the major product, and poor CO selectivity. In contrast, Rh@Beta exhibited much higher CO selectivity. Supplementary Figs. 50c,d and 51b show the data characterizing the performance of various catalysts in the hydrogenation of  $\text{CO}_2$  at 350 °C. The average rates of the reaction on Rh/ $\text{Al}_2\text{O}_3$ -com and Rh/Beta decreased markedly at the beginning of the reaction in the flow reactor, being 41.8 and 75.1  $\text{mol}_{\text{CO}_2} \text{mol}_{\text{Rh}}^{-1} \text{h}^{-1}$  after reaction for 1,200 min on

Rh/ $\text{Al}_2\text{O}_3$ -com and Rh/Beta, respectively. These reaction rates are much lower than the values of 118 and 160  $\text{mol}_{\text{CO}_2} \text{mol}_{\text{Rh}}^{-1} \text{h}^{-1}$  characterizing the as-synthesized Rh/ $\text{Al}_2\text{O}_3$ -com and Rh/Beta catalysts because of the rhodium nanoparticle aggregation evidenced by the TEM images (Supplementary Figs. 52 and 53). A calcination step led to partial regeneration of Rh/ $\text{Al}_2\text{O}_3$ -com and Rh/Beta, and the average reaction rates increased to 105 and 125  $\text{mol}_{\text{CO}_2} \text{mol}_{\text{Rh}}^{-1} \text{h}^{-1}$ , respectively. However, these values are much lower than those characterizing the fresh catalysts (Supplementary Figs. 50d and 51b). Importantly, Rh@Beta displayed stable catalytic performance over a long reaction period of 6,000 min (Supplementary Fig. 50c), and rhodium nanoparticles were almost unchanged in size after the test (Supplementary Fig. 54), again confirming the superior stability of the Rh@Beta catalyst.

## Discussion

The reported data show that zeolite-encapsulated supported catalysts prepared using metal-nanoparticle-containing zeolite seeds are valuable in practical applications. Metal@zeolite catalysts offer remarkable advantages over conventional zeolite-supported metal catalysts, as they are obtained without the use of organic stabilizers or templates, and feature superior performance, especially in terms of catalyst stability associated with the sinter resistance properties of the final composite. A key to the stabilization of these nanoparticles is the crystallization process: the metal nanoparticles on the surfaces of the zeolite seeds are covered and isolated by an amorphous aluminosilicate gel that prevents nanoparticle aggregation during the crystallization process and further results in a crystalline zeolite sheath that stabilizes the nanoparticles even during operation under severe conditions. It is significant that this synthesis method allows control of the metal nanoparticle sizes in the typical range required for industrial catalysts—in fact, the nanoparticles that are formed on the zeolite seeds retain their sizes in the subsequent preparation steps, protected by the sheath. The most important advantage of metal@zeolite catalysts over conventional supported metal catalysts is the resistance of the metals to sintering, even under harsh conditions. The advantages pertain to a whole set of industrial reactions, including the WGS reaction, CO oxidation, oxidative reforming of methane and  $\text{CO}_2$  hydrogenation (Fig. 1), and are quite general. We anticipate that the method can be extended to supported catalysts other than metals, such as those containing nanoparticles of metal sulphides and metal oxides.

## Methods

**Catalyst preparation.** The metal nanoparticles fixed inside zeolite crystals (Pt@Beta, Pt@MOR, Rh@Beta, Rh@MOR, Ag@Beta, Ag@MOR, Pt@Beta-Fe and Pd@S-1) were synthesized by a two-step process. For example, in the synthesis of Pt@Beta, commercially available zeolite Beta crystals (Si/Al ~12.5) with diameters in the range of 150–410 nm were used as the zeolite Beta seeds. In a typical preparation, 1.0 g of commercial zeolite Beta was mixed with 2.05 ml of aqueous  $\text{H}_2\text{PtCl}_6$  solution (0.05 M). The mixture was subjected to ultrasound for 1 h at room temperature, followed by aging at room temperature overnight, drying at 80 °C for 4 h, calcination at 400 °C for 4 h in air, and reduction at 300 °C in 10%  $\text{H}_2/\text{Ar}$  for 2 h to give platinum-containing zeolite Beta (Pt/Beta) seeds with a platinum loading of 2.0 wt%. Separately, an aluminosilicate gel with a molar ratio of  $\text{Na}_2\text{O}:\text{Al}_2\text{O}_3:\text{SiO}_2:\text{H}_2\text{O}$  of 11:1:26:270 was prepared using 0.64 g of  $\text{NaAlO}_2$ , 1.12 g of NaOH, 4.0 g of fumed silica and 13.6 g of water as the raw materials. After stirring for 12 h, 0.4 g of platinum-containing zeolite Beta seeds (Pt/Beta seeds, 10 wt% based on the  $\text{SiO}_2$  source) was introduced into the gel for hydrothermal crystallization at 120 °C for 3 days or at 140 °C for 32 h. After filtration, washing with water and drying, the product Pt@Beta was obtained. The platinum loading of Pt@Beta was 0.41 wt%, which is much lower than that of the Pt/Beta seeds. Pt@MOR was obtained using the same procedures, except the hydrothermal treatment was performed at 140 °C for 4 days. By changing the metal precursors, Rh@Beta, Rh@MOR, Ag@Beta and Ag@MOR were also prepared following the same route.

In a typical synthesis of Pd@S-1 seeds, we used a molar ratio of tetrapropylammonium hydroxide (TPAOH): $\text{SiO}_2:\text{H}_2\text{O}$  of 0.2:1:60 by stirring 2.08 g of tetraethyl orthosilicate, 1.02 g of TPAOH (40 wt%; BASF) and 10.8 g of  $\text{H}_2\text{O}$  at room temperature for 5 h, followed by hydrothermal treatment at 180 °C for 3 days. The S-1 seeds were obtained after centrifugation, washing with a large

excess of water, drying at 80 °C overnight and calcination at 550 °C for 4 h (ramp rate: 1 °C min<sup>-1</sup>) in air. Then, 1 g of the as-synthesized S-1 zeolite was dried under vacuum at 120 °C for 4 h, followed by mixing with 4.7 ml of aqueous Na<sub>2</sub>PdCl<sub>4</sub> solution (0.05 M). The mixture was subjected to ultrasound for 1 h at room temperature, followed by aging overnight. The water was removed by heating to 60 °C and holding for 12 h, followed by 80 °C for 4 h. After calcination at 400 °C for 4 h with a ramp rate of 1 °C min<sup>-1</sup> in static air, then reduction at 300 °C for 2 h with a ramp rate of 5 °C min<sup>-1</sup> in 10% H<sub>2</sub>/Ar (flow rate: 50 ml min<sup>-1</sup>), Pd/S-1 seeds with a palladium loading of 2.5 wt% were obtained.

In a typical synthesis of Pd@S-1, a solid mixture with a molar ratio of TPAOH: Pd/S-1 seeds: SiO<sub>2</sub>: H<sub>2</sub>O of 0.065: 0.67: 1: 1.1 was obtained by grinding 1.0 g of Pd/S-1 seeds with 1.5 g of fumed silica and 0.83 g of TPAOH (40 wt%: BASF). After grinding for 20 min, the resultant powder was transferred to an autoclave for thermal treatment at 180 °C for 3 days. The sample was collected by washing with large excess of water followed by drying at 80 °C overnight. After calcination at 550 °C for 4 h (ramp rate: 1 °C min<sup>-1</sup>) in static air and reduction at 300 °C in 10% H<sub>2</sub>/Ar (flow rate: 50 ml min<sup>-1</sup>) for 2 h, the product Pd@S-1 was obtained.

**Characterization.** X-ray diffraction patterns were collected on a Rigaku D/Max 2550 diffractometer with Cu K $\alpha$  radiation ( $\lambda = 1.5418 \text{ \AA}$ ). Metal contents were determined by inductively coupled plasma analysis (3300DV; PerkinElmer). Nitrogen sorption isotherms were measured using a Micromeritics ASAP 2020 system. The samples were ion exchanged into the H form before the tests. Some of the TEM and STEM images were obtained on a JEM-2100F electron microscope (JEOL) with an acceleration voltage of 200 kV. Other phase-contrast TEM, STEM and electron diffraction measurements were performed using a Tecnai F30 S-TWIN transmission electron microscope equipped with a field emission gun and operating at 300 kV (an FEI Titan probe corrector electron microscope operated at 300 kV was employed for the data in Supplementary Video 3). The tilt series images were taken from  $-70^\circ$  to  $+70^\circ$  with a tilt increment of  $1-2^\circ$ . The tilt series images were first aligned and then reconstructed to a 3D volume using the SIRT function of FEI Inspect 3D software (<https://www.fei.com/software/inspect-3d/>). Further 3D volume rendering, density segmentation and isosurface construction were achieved with Avizo software (<https://www.fei.com/software/amira-avizo/>). SEM experiments were performed with Hitachi SU8010 electron microscopes. The errors in metal nanoparticle size measurements are within  $\pm 0.2 \text{ nm}$ . Thermal gravimetric analysis experiments were performed on an SDT Q600 V8.2 Build 100 thermogravimetric analyser under air flow with a ramp rate of  $10^\circ \text{ C min}^{-1}$ . X-ray photoelectron spectra were obtained with a Thermo Fisher Scientific ESCALAB 250Xi photoelectron spectroscopy system using a monochromatic Al K $\alpha$  (1,486.6 eV) X-ray source. The binding energy values were calibrated using the C 1s peak at 284.9 eV.

**Catalytic reaction tests.** WGS reactions were carried out using a fixed-bed reactor with a diameter of 4 mm at atmospheric pressure. The reactor was mounted in a temperature-controlled oven. The catalysts (commercial catalysts were ground into powders before use) were pressed, crushed, sieved into particles with a mesh size of 40–60 and mixed with inert quartz particles in a volume ratio of 1:1. The reactor was heated in flowing He to 200 °C before the reactant gas flow was started. Water was injected by a pump, then evaporated and mixed with the dry gas to ensure that the gas composition was 15% CO + 5% CO<sub>2</sub> + 30% H<sub>2</sub>O + 40% H<sub>2</sub> + 10% He. The tests were performed at a gas hourly space velocity (GHSV) of 1,875,000 ml g<sub>pt</sub><sup>-1</sup> h<sup>-1</sup>. After it was passed through a condenser to remove the water, the product gas was analysed using gas chromatographs equipped with a thermal conductivity detector (TCD) and a flame ionisation detector (FID). Average reaction rates were calculated from the number of moles of CO converted per mole of platinum species (total amount of platinum species in the reactor) in one hour. The deactivated catalyst was regenerated with 20% O<sub>2</sub>/He at 400 °C for 2 h and 10% H<sub>2</sub>/Ar at 400 °C for 2 h.

CO oxidation was carried out in the same reactor as was used for the WGS reaction. The catalysts were pressed, crushed, sieved into 40–60-mesh-size particles and mixed with quartz particles in a volume ratio of 1:1. The catalyst particles were placed in the middle part of the reactor, then pretreated with flowing 20% O<sub>2</sub>/He at 200 °C for 1 h. A gas composition of 1% CO + 19% O<sub>2</sub> + 80% He was used as feed with a GHSV of 120,000 ml g<sub>pt</sub><sup>-1</sup> h<sup>-1</sup> for platinum catalysts and a feed gas composition of 0.1% CO + 19% O<sub>2</sub> + 80.9% He with a GHSV of 120,000 ml g<sub>Ag</sub><sup>-1</sup> h<sup>-1</sup> was used for silver catalysts. The product gas streams were analysed with a gas chromatograph equipped with a TCD. The deactivated catalyst was regenerated with flowing 20% O<sub>2</sub>/He at 200 °C for 2 h.

Oxidative reforming of methane to syngas was carried out with the same reactor. The catalysts (commercial catalysts were ground into powders before use) were pressed, crushed, sieved into 40–60-mesh-size particles and mixed with quartz at a volume ratio of 1:1. The catalyst particles were placed in the middle part of the reactor. The catalyst was pretreated with 20% O<sub>2</sub>/He at 600 °C flowing for 1 h. Gas with a composition of 7% CH<sub>4</sub> + 3.3% O<sub>2</sub> + 89.7% He as feed was introduced into the reactor with a GHSV of 480,000 ml g<sub>cat</sub><sup>-1</sup> h<sup>-1</sup>. The product gas was analysed using two gas chromatographs—one equipped with a TCD and the other with a FID. The deactivated catalysts were regenerated with flowing 20% O<sub>2</sub>/He at 600 °C for 4 h.

Hydrogenation of CO<sub>2</sub> was carried out in the same reactor. The catalysts (commercial catalysts were ground into powders before use) were pressed, crushed, sieved into 40–60-mesh-size particles and mixed with quartz particles at a volume ratio of 1:1. The catalyst was placed in the middle part of the reactor and pretreated with flowing H<sub>2</sub> at 500 °C for 1 h. Feed gas with a composition of 9.4% CO<sub>2</sub> + 37.5% H<sub>2</sub> + 53.1% He was introduced into the reactor with a GHSV of 1,920,000 ml g<sub>rh</sub><sup>-1</sup> h<sup>-1</sup>. The product gas was analysed using two gas chromatographs—one equipped with a TCD and the other with an FID. The deactivated catalysts were regenerated by calcination in flowing 20% O<sub>2</sub>/He at 500 °C for 2 h and reduction in H<sub>2</sub> at 500 °C for 1 h for the next run.

**Data availability.** The data that support the plots within this paper and other findings of this study are available from the corresponding author upon reasonable request.

Received: 28 August 2017; Accepted: 24 May 2018;  
Published online: 9 July 2018

## References

- Ertl, G., Knözinger, H., Schüth, F. & Weitkamp, J. *Handbook of Heterogeneous Catalysis* (Wiley, Weinheim, 2008).
- Behrens, M. et al. The active site of methanol synthesis over Cu/ZnO/Al<sub>2</sub>O<sub>3</sub> industrial catalysts. *Science* **336**, 893–897 (2012).
- Lu, J. et al. Coking- and sintering-resistant palladium catalysts achieved through atomic layer deposition. *Science* **335**, 1205–1208 (2012).
- Li, W.-Z. et al. Stable platinum nanoparticles on specific MgAl<sub>2</sub>O<sub>4</sub> spinel facets at high temperatures in oxidizing atmospheres. *Nat. Chem.* **4**, 2481 (2013).
- Prieto, G., Zečević, J., Friedrich, H., de Jong, K. P. & de Jongh, P. E. Towards stable catalysts by controlling collective properties of supported metal nanoparticles. *Nat. Mater.* **12**, 34–39 (2013).
- Tang, H. et al. Strong metal–support interactions between gold nanoparticles and nonoxides. *J. Am. Chem. Soc.* **138**, 56–59 (2016).
- Ta, N. et al. Stabilized gold nanoparticles on ceria nanorods by strong interfacial anchoring. *J. Am. Chem. Soc.* **134**, 20585–20588 (2012).
- Zhao, M.-Q. et al. Embedded high density metal nanoparticles with extraordinary thermal stability derived from guest–host mediated layered double hydroxides. *J. Am. Chem. Soc.* **132**, 14739–14741 (2010).
- Tang, H. et al. Ultrastable hydroxyapatite/titanium-dioxide-supported gold nanocatalyst with strong metal–support interaction for carbon monoxide oxidation. *Angew. Chem. Int. Ed.* **55**, 10606–10611 (2016).
- Sattler, J. J. H. B. et al. Platinum-promoted Ga/Al<sub>2</sub>O<sub>3</sub> as highly active, selective, and stable catalyst for the dehydrogenation of propane. *Angew. Chem. Int. Ed.* **53**, 9251–9256 (2014).
- Zhang, L. Y. et al. Stabilization of palladium nanoparticles on nanodiamond–graphene core–shell supports for CO oxidation. *Angew. Chem. Int. Ed.* **54**, 15823–15826 (2015).
- Shi, L. et al. Al<sub>2</sub>O<sub>3</sub> nanosheets rich in pentacoordinate Al<sup>3+</sup> ions stabilize Pt–Sn clusters for propane dehydrogenation. *Angew. Chem. Int. Ed.* **54**, 13994–13998 (2015).
- Wang, S. et al. Aggregation-free gold nanoparticles in ordered mesoporous carbons: toward highly active and stable heterogeneous catalysts. *J. Am. Chem. Soc.* **135**, 11849–11860 (2013).
- Zhou, H. P. et al. Thermally stable Pt/CeO<sub>2</sub> hetero-nanocomposites with high catalytic activity. *J. Am. Chem. Soc.* **132**, 4998–4999 (2010).
- Farrauto, R. J. & Bartholomew, C. H. *Fundamentals of Industrial Catalytic Process* (Blackie, London, 1997).
- Morgan, K., Goguet, A. & Hardacre, C. Metal redispersion strategies for recycling of supported metal catalysts: a perspective. *ACS Catal.* **5**, 3430–3445 (2015).
- Dick, K., Dhanasekaran, T., Zhang, Z. Y. & Meisel, D. Size-dependent melting of silica-encapsulated gold nanoparticles. *J. Am. Chem. Soc.* **124**, 2312–2317 (2002).
- Joo, S. H. et al. Thermally stable Pt/mesoporous silica core–shell nanocatalysts for high-temperature reactions. *Nat. Mater.* **8**, 126–131 (2009).
- Yu, K., Wu, Z. C., Zhao, Q. R., Li, B. X. & Xie, Y. High-temperature-stable Au@SnO<sub>2</sub> core/shell supported catalyst for CO oxidation. *J. Phys. Chem. C* **112**, 2244–2247 (2008).
- Cargnello, M. et al. Exceptional activity for methane combustion over modular Pd@CeO<sub>2</sub> subunits on functionalized Al<sub>2</sub>O<sub>3</sub>. *Science* **337**, 713–717 (2012).
- Arnal, P. M., Comotti, M. & Schüth, F. High-temperature-stable catalysts by hollow sphere encapsulation. *Angew. Chem. Int. Ed.* **45**, 8224–8227 (2006).
- O'Neill, B. J. et al. Stabilization of copper catalysts for liquid-phase reactions by atomic layer deposition. *Angew. Chem. Int. Ed.* **52**, 13808–13812 (2013).
- Zhan, W. et al. A sacrificial coating strategy toward enhancement of metal–support interaction for ultrastable Au nanocatalysts. *J. Am. Chem. Soc.* **138**, 16130–16139 (2016).

24. Huang, W. et al. Low-temperature transformation of methane to methanol on Pd<sub>2</sub>O<sub>4</sub> single sites anchored on the internal surface of microporous silicate. *Angew. Chem., Int. Ed.* **55**, 13441–13445 (2016).
25. Laursen, A. B. et al. Substrate size-selective catalysis with zeolite-encapsulated gold nanoparticles. *Angew. Chem. Int. Ed.* **49**, 3504–3507 (2010).
26. Goel, S., Wu, Z., Zones, S. I. & Iglesia, E. Synthesis and catalytic properties of metal clusters encapsulated within small-pore (SOD, GIS, ANA) zeolites. *J. Am. Chem. Soc.* **134**, 17688–17695 (2012).
27. Wang, N. et al. In situ confinement of ultrasmall Pd clusters within nanosized silicalite-1 zeolite for highly efficient catalysis of hydrogen generation. *J. Am. Chem. Soc.* **138**, 7484–7487 (2016).
28. Liu, L. et al. Generation of subnanometric platinum with high stability during transformation of a 2D zeolite into 3D. *Nat. Mater.* **16**, 132–138 (2017).
29. Bond, G. C., Louis, C. & Thompson, D. T. *Catalysis by Gold* (Imperial College Press, London, 2006).
30. Iglesias-Juez, A., Kubacka, A., Fernández-García, M., Michiel, M. D. & Newton, M. A. Nanoparticulate Pd supported catalysts: size-dependent formation of Pd(I)/Pd(0) and their role in CO elimination. *J. Am. Chem. Soc.* **133**, 4484–4489 (2011).
31. Xiao, F. S., Weber, W. A., Alexeev, O. & Gates, B. C. Probing the limits of structure insensitivity: size-dependent catalytic activity of Al<sub>2</sub>O<sub>3</sub>-supported iridium clusters and particles for toluene hydrogenation. *Stud. Surf. Sci. Catal.* **101**, 1135–1144 (1996).
32. Kistler, J. D. et al. A single-site platinum CO oxidation catalyst in zeolite KLT: microscopic and spectroscopic determination of the locations of the platinum atoms. *Angew. Chem. Int. Ed.* **53**, 8904–8907 (2014).
33. Cui, T.-L. et al. Encapsulating palladium nanoparticles inside mesoporous MFI zeolite nanocrystals for shape-selective catalysis. *Angew. Chem. Int. Ed.* **55**, 9178–9182 (2016).
34. Wang, C. et al. Product selectivity controlled by zeolite crystals in biomass hydrogenation over a palladium catalyst. *J. Am. Chem. Soc.* **138**, 7880–7883 (2016).
35. Sachtler, W. M. H. Metal clusters in zeolites: an intriguing class of catalysts. *Acc. Chem. Res.* **26**, 383–387 (1993).
36. Sun, T. & Seff, K. Silver clusters and chemistry in zeolites. *Chem. Rev.* **94**, 857–870 (1994).
37. Guzman, J. in *Model Systems in Catalysis* (ed. Rioux, R.) Ch. 19 (Springer, New York, 2010).
38. Creighton, E. J. & Downing, R. S. Shape-selective hydrogenation and hydrogen transfer reactions over zeolite catalysts. *J. Mol. Catal. A* **134**, 47–61 (1998).
39. Alexeev, O. S. & Gates, B. C. Supported bimetallic cluster catalysts. *Ind. Eng. Chem. Res.* **42**, 1571–1587 (2003).
40. Yamamoto, T., Shido, T., Inagaki, S., Fukushima, Y. & Ichikawa, M. Ship-in-bottle synthesis of [Pt<sub>15</sub>(CO)<sub>30</sub>]<sup>2-</sup> encapsulated in ordered hexagonal mesoporous channels of FSM-16 and their effective catalysis in water-gas shift reaction. *J. Am. Chem. Soc.* **118**, 5810–5811 (1996).
41. Rodriguez, J. A. et al. Activity of CeO<sub>x</sub> and TiO<sub>x</sub> nanoparticles grown on Au(111) in the water-gas shift reaction. *Science* **318**, 1757–1760 (2007).
42. Yang, M. et al. Catalytically active Au–O(OH)<sub>x</sub> species stabilized by alkali ions on zeolites and mesoporous oxides. *Science* **346**, 1498–1501 (2014).
43. Yang, M. et al. A common single-site Pt(II)–O(OH)<sub>x</sub> species stabilized by sodium on “active” and “inert” supports catalyzes the water-gas shift reaction. *J. Am. Chem. Soc.* **137**, 3470–3473 (2015).
44. Chen, M. S., Cai, Y., Yan, Z. & Goodman, D. W. On the origin of the unique properties of supported Au nanoparticles. *J. Am. Chem. Soc.* **128**, 6341–6346 (2006).
45. Ouyang, R. & Li, W.-X. Adsorbed CO induced change of the adsorption site and charge of Au adatoms on FeO(111)/Ru(0001). *Chin. J. Catal.* **34**, 1820–1825 (2013).
46. Fu, Q. et al. Interface-confined ferrous centers for catalytic oxidation. *Science* **328**, 1141–1144 (2010).
47. Chen, G. et al. Interfacial effects in iron–nickel hydroxide–platinum nanoparticles enhance catalytic oxidation. *Science* **344**, 495–499 (2014).
48. Hickman, D. A. & Schmidt, L. D. Production of syngas by direct catalytic oxidation of methane. *Science* **259**, 343–346 (1993).
49. Ayabe, S. et al. Catalytic autothermal reforming of methane and propane over supported metal catalysts. *Appl. Catal. A* **241**, 261–269 (2003).
50. Carrasquillo-Flores, R. et al. Reverse water-gas shift on interfacial sites formed by deposition of oxidized molybdenum moieties onto gold nanoparticles. *J. Am. Chem. Soc.* **137**, 10317–10325 (2015).

### Acknowledgements

This work is supported by the National Key Research and Development Program of China (2018YFB060128) and National Natural Science Foundation of China (91645105, 91634201 and 21720102001). L.W. gratefully acknowledges the Natural Science Foundation of Zhejiang Province (LR18B030002). B.C.G. acknowledges financial support from the US Department of Energy, Office of Science, Basic Energy Sciences (grant DE-FG02-04ER15513). H.Z. acknowledges financial support from the Carl-Zeiss-Stiftung. The work reported in this paper is protected by Chinese patents (application numbers 201610342078.0 and 201610341082.5).

### Author Contributions

J.Z. performed the catalyst preparation, characterizations and catalytic tests. G.W. and C.W. performed the catalytic tests. B.Z., D.S.S., H.Z., U.K., Y.Z., L.L. and Y.H. performed the TEM characterization. B.C.G. performed the data analysis and offered helpful suggestions. L.W. and F.-S.X. designed this study, analysed the data and wrote the paper.

### Competing interests

The authors declare no competing interests.

### Additional information

**Supplementary information** is available for this paper at <https://doi.org/10.1038/s41929-018-0098-1>.

**Reprints and permissions information** is available at [www.nature.com/reprints](http://www.nature.com/reprints).

**Correspondence and requests for materials** should be addressed to L.W. or F.-S.X.

**Publisher's note:** Springer Nature remains neutral with regard to jurisdictional claims in published maps and institutional affiliations.